J Mater Sci (2006) 41:5346–5358
DOI 10.1007/s10853-006-0327-x

Effect of oxygen injection on synthesizing barium titanate nanoparticles by plasma chemical vapor deposition

Keigo Suzuki · Kazunori Kijima

Received: 13 August 2004 / Accepted: 15 September 2005 / Published online: 6 June 2006

Abstract Nanoparticles of barium titanate were prepared by plasma chemical vapor deposition using an inductively coupled plasma technique that has a high potential for preparing nanoparticles. The present paper describes the details of the reaction control achieved by accelerating the reactions between Ba atoms and oxygen using direct injection of oxygen into the tail of the plasma flame. According to our previous reports, the crystalline phases of the powder products were different at each collection area in the CVD apparatus. This was due to the remaining active Ba atoms without a reaction in the plasma tail flame, as observed from the optical emission spectroscopy. After the reactions between Ba atoms and oxygen occurred by direct oxygen injection, $BaTiO_3$ perovskite phases were produced as a major phase in each collection area. The optimal oxygen injecting conditions for obtaining perovskite $BaTiO_3$ single phase are summarized as follows: the temperature of the plasma tail flame at oxygen-injecting position = approximately 1000 K and molar ratio of oxygen to the reactants (O_2/(Ba+Ti)) = 4000. Furthermore, $BaTiO_3$ nanoparticles with average particle size under 10 nm were prepared by oxygen injection (the average particle size without oxygen injection is 15.4 nm). Well-crystallized $BaTiO_3$ nanoparticles with spherical shape were observed by TEM.

K. Suzuki (✉)
Murata Manufacturing Co. Ltd., 2288, Oshinohara,
Yasu-shi, Shiga, Japan
e-mail: ksuzuki@murata.co.jp

K. Kijima
Graduate School of Materials Science and Technology, Kyoto Institute of Technology, Matsugasaki, Sakyo-ku, Kyoto, Japan

Introduction

Since T.B. Reed first succeeded in generating high-temperature plasma by inductively coupling (ICP) [1], and applied it to chemical vapor deposition (RF-plasma CVD), this technique has been utilized as a powerful method for preparing ceramic nanoparticles. Since ICP is electrodeless plasma, highly pure ceramic nanoparticles can be obtained by RF-plasma CVD. Hitherto, numerous kinds of ceramic nanoparticles such as carbide, nitride and oxide have been synthesized by the RF-plasma CVD method. The production of carbide and nitride nanoparticles such as SiC [2–4], TaC [5] and Si_3N_4 [6] has been reported. With regard to oxide nanoparticles, M. Kagawa et al. have produced a wide variety of nanoparticles such as MgO [7, 8], CeO_2 [7, 9], Fe_2O_3 [7, 10], ZrO_2 [7] etc., using liquid reactants as starting materials. Moreover, multi-component oxide nanoparticles such as Al_2O_3–SiO_2 [11], Al_2O_3–TiO_2 [12], Al_2O_3–Cr_2O_3 [13, 14], Al_2O_3–ZrO_2 [15, 16], CrO_2–TiO_2 [17], SiO_2–ZrO_2 [18], Y–Al–O [19] and Y–Fe–O [20] have been prepared using RF-plasma CVD techniques.

Recently, we succeeded in preparing barium titanate ($BaTiO_3$) nanoparticles, which is one of the multi-component oxides, by RF-plasma CVD using metalorganic sources as starting materials [21, 22]. Well-crystallized $BaTiO_3$ nanoparticles of approximately 15 nm were obtained by the method. However, a problem exists for collecting the $BaTiO_3$ nanoparticles by RF-plasma CVD under the previous experimental conditions [21, 22]. Crystalline phases of the products are observed to be different in each collection area. Powder products with perovskite $BaTiO_3$ phase are deposited on the chamber wall, whereas barium compounds such as barium nitrate ($Ba(NO_3)_2$) are obtained from a product collection vessel, placed just below the plasma tail flame. These results imply

that the plasma CVD process cannot be completely controlled under the previous experimental condition. This is a problem for industrial applications as well as science.

Previous studies using optical emission spectroscopy confirmed that excess barium (Ba) atoms remained in the plasma tail flame [22]. The production of barium compounds in the collection vessel was considered to be due to the remaining Ba atoms. Ba atoms should react completely with other elements in the plasma tail flame to prevent a generation of barium compounds in the vessel. According to this viewpoint, it is assumed that an increase of the oxygen concentration in the system would be effective. However, introduction of large amounts of oxygen molecules into the ICP flame causes instability in the ICP flame, because the dissociation of oxygen molecules requires a significant amount of energy in the ICP.

Therefore, in the present study, oxygen concentration was increased by means of direct oxygen injection into the plasma tail flame. The effect of oxygen injection on powder properties was investigated in detail.

Experimental

Figure 1 shows a schematic drawing of the experimental apparatus. ICP was generated in a fused-silica reaction tube using an RF generator with 4 MHz of frequency and 15 kW of maximum output power (Model NTU-1506A, International Electric, Tokyo, Japan). Titanium iso-propoxide ($Ti(OiPr)_4$, >95% purity) (Nacalai Tesque Inc., Kyoto, Japan) and bis-dipivaloylmethanate barium ($Ba(DPM)_2$, 98% purity) (Kojundo Chemical Laboratory Co., Saitama, Japan) were used as source materials. A mixture of $Ba(DPM)_2$ and $Ti(OiPr)_4$ was introduced into the ICP flame with an argon (Ar) carrier gas through the central injection pipe of a plasma torch. Details of plasma generation and introduction of source materials are described in previous papers [21, 22]. The experimental condition of the present study is summarized in Table 1.

Figure 2(a) shows a schematic drawing of the top view of the reaction chamber. Oxygen was injected from the periphery to the center of the plasma tail flame using a 1/4″ stainless steel tube inclined at an angle of 90°. Table 2 shows the oxygen injection conditions in the present experiment. Oxygen-injecting positions and oxygen flow rates were varied as experimental parameters. A mixture of Ar (200 SCCM) and oxygen (1000 SCCM) together with oxygen injection into the plasma tail flame was introduced into the ICP as a working gas, which was kept constant for all experimental conditions (see Table 1).

Figure 2(b) shows the 3 powder collection areas. The chamber wall (CW) was divided into two sections, upper (CWU) and lower (CWL). The vessel (VES), just below the plasma tail flame, was used for collecting powder products. A water-cooled vessel was used for powder collection. The powder products collected from CWU, CWL and VES are defined as CWU products, CWL products and VES products, respectively. These products were collected and characterized separately.

The synthesized phase of the powder products was identified by powder X-ray diffraction (XRD) (Model RINT2000, RIGAKU, Tokyo, Japan) using CuK_α radiation (0.154051 nm, 40 kV, 50 mA). The morphology was investigated using a transmission electron microscope (TEM) (Model EM-002B, TOPCON, Tokyo, Japan). The Ba/Ti atomic ratio of the products was estimated by X-ray fluorescence (XRF) (Model ZSX100E, RIGAKU, Tokyo, Japan) using RhK_α radiation (0.061324 nm 50 kV, 70 mA).

Results

Crystalline phases without oxygen injection into the plasma tail flame

Figure 3 shows an XRD pattern of the powder products prepared without oxygen injection into the plasma tail flame. In this case, oxygen (1000 SCCM) was introduced into the ICP as a working gas. The perovskite $BaTiO_3$ phase was obtained at the collection areas of CWU and CWL. The Ba/Ti atomic ratios of the CWU products and CWL products were estimated to be 1.00 and 0.95, respectively (using XRF). In contrast, the $Ba(NO_3)_2$ phase was obtained as VES products. The Ba/Ti atomic ratio of the VES products was calculated to be 1.21 (using XRF), indicating that the amounts of Ti atoms included in the VES products were almost equal to those of Ba atoms. Accordingly, the Ti elements are speculated to exist as an amorphous phase in the VES products.

It is speculated that $Ba(NO_3)_2$ obtained from the VES is not formed in the plasma tail flame, because no nitrogen elements are included in the raw materials. As reported in the previous paper [22], excess Ba atoms remain in the plasma tail flame. The mechanism of the formation of the $Ba(NO_3)_2$ phase is supposed as follows: active Ba atoms were deposited on the water-cooled vessel during the reaction. Subsequently, these active Ba atoms reacted with nitrogen and oxygen, then transformed to the $Ba(NO_3)_2$ phase, when the reaction chamber was exposed to air for collecting the products. This phenomenon will be discussed in detail in the section The effect of oxygen injection on the crystalline phase.

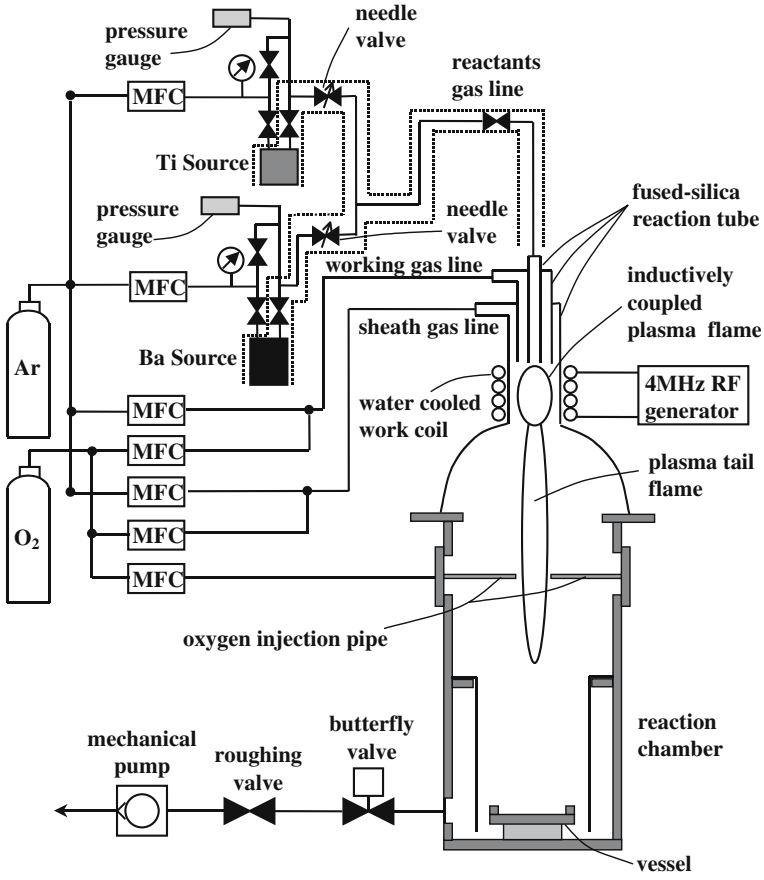

Fig. 1 A schematic drawing of the experimental apparatus. The inductively coupled plasma was generated by a 4 MHz radio frequency generator with a maximum output power of 15 kW using four turned copper work coil. $Ba(DPM)_2$ and $Ti(OiPr)_4$ were used as source materials, and were introduced into the inductively coupled plasma flame

Crystalline phases with oxygen injection into the plasma tail flame

Figure 4 shows the XRD patterns of the powder products prepared by oxygen injection into the plasma tail flame. In this case, oxygen (1000 SCCM) was introduced into the ICP as a working gas. Figure 4(a) shows the XRD patterns of the products prepared under the following conditions: oxygen-injected position = 340 mm below the center of ICP and oxygen flow rate = 3500 SCCM. Figure 4(b) shows the XRD patterns of the products prepared under the following condition: oxygen-injected position = 520 mm below the ICP and oxygen flow rate = 3500 SCCM. As shown in Fig. 4, an almost single phase of perovskite $BaTiO_3$ was obtained from all the collection areas (CWU, CWL and VES). The perovskite $BaTiO_3$ phase was observed as a major phase in each collection area under all the conditions shown in Table 2.

The fraction of the crystalline phases of the products from each collection area was calculated from XRD peak intensities using the internal standard method. It should be noted that broad peaks were found at $2\theta = 20°–30°$ in the XRD patterns except for the crystalline phases such as $BaTiO_3$, $BaCO_3$ and $Ba(NO_3)_2$ (Fig. 4). This indicates that an amorphous phase other than the crystalline phases exists in the products. However, the peaks due to the amorphous phase were rather weak and broad, therefore it was difficult to quantify the fraction of the amorphous phases.

Hence, in the present study, curve-fitting of the XRD peaks in the calculation was performed against the peaks that originated from the crystalline phases, such as $BaTiO_3$, $BaCO_3$ and $Ba(NO_3)_2$. The fraction of the amorphous phases was neglected in the curve-fitting. The average

Table 1 Experimental conditions for synthesizing $BaTiO_3$ nanoparticles by plasma CVD

Barium source $(BaDPM)_2$)	
Heating temperature	523 K
Ar carrier gas flow rate	700 SCCM
Pressure of source cylinder	6.65 kPa
Titanium source $(Ti(OiPr)_4)$	
Heating temperature	315 K
Ar carrier gas flow rate	90 SCCM
Pressure of source cylinder	5.98 kPa
Ar working gas flow rate	200 SCCM
O_2 working gas flow rate	1000 SCCM
Sheath gas flow rate	4500 SCCM
Output power	6.0 kW
Total gaseous pressure	4.0 kPa
Duration time	120 min
Product collection vessel	water cooled vessel

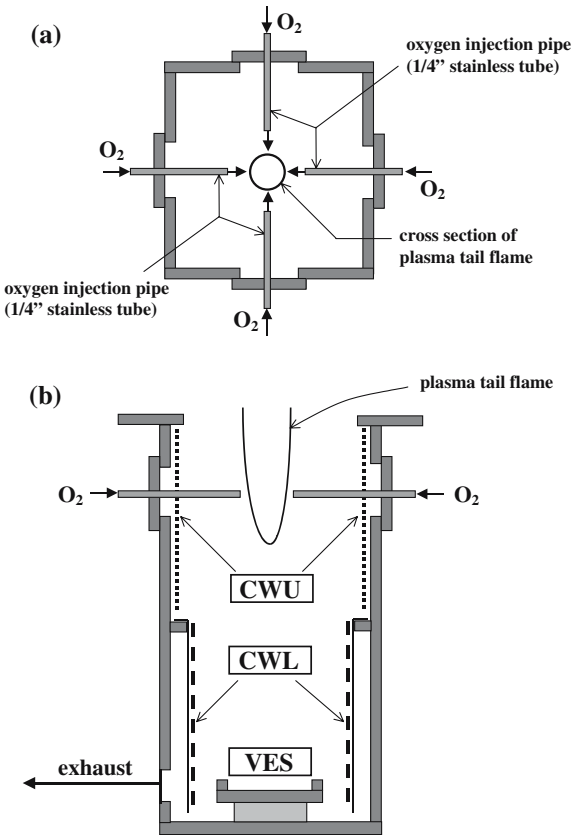

Fig. 2 A detail of the reaction chamber. (a) Top view of the chamber. Oxygen was injected from the periphery to the center of the plasma tail flame using a 1/4″ stainless steel tube inclined at an angle of 90°. (b) The powder collection areas. The chamber wall (CW) was divided into two sections, upper (CWU) and lower (CWL). The vessel (VES) just below the plasma tail flame was also used for collecting powder products. These powder products were collected and characterized separately

fraction of a crystalline phase, such as the $BaTiO_3$ phase, was calculated by the following equation.

$$\begin{aligned} AVR_{BT} &= F_{BT-CWU} \cdot X_{CWU} + F_{BT-CWL} \cdot X_{CWL} \\ &\quad + F_{BT-VES} \cdot X_{VES} \end{aligned} \tag{1}$$

Here, AVR_{BT}, F_{BT-CWU}, X_{CWU}, F_{BT-CWL}, X_{CWL}, F_{BT-VES} and X_{VES} represent the average $BaTiO_3$ phase fraction, the $BaTiO_3$ phase fraction in the CWU product, the weight ratio of the CWU product, the $BaTiO_3$ phase fraction in the CWL product, the weight ratio of the CWL product, the $BaTiO_3$

Table 2 Conditions of oxygen injection for synthesizing $BaTiO_3$ nanoparticles by plasma CVD. The value of the oxygen-injected position represents the distance between the ICP and oxygen-injected position

Injected oxygen flow rate2000 SCCM, 3500 SCCM, 5000 SCCM
Oxygen-injected position 160 mm, 340 mm, 520 mm below the ICP

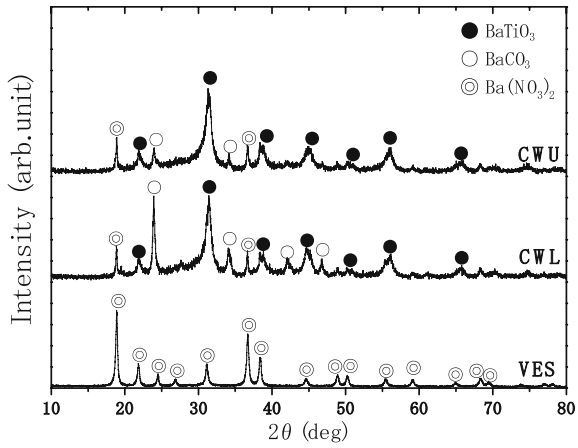

Fig. 3 XRD patterns of the powder products obtained without oxygen injection into the plasma tail flame (CuK_α). In this case, oxygen (1000 SCCM) was introduced into the ICP as a working gas. A water-cooled vessel was used for powder collection

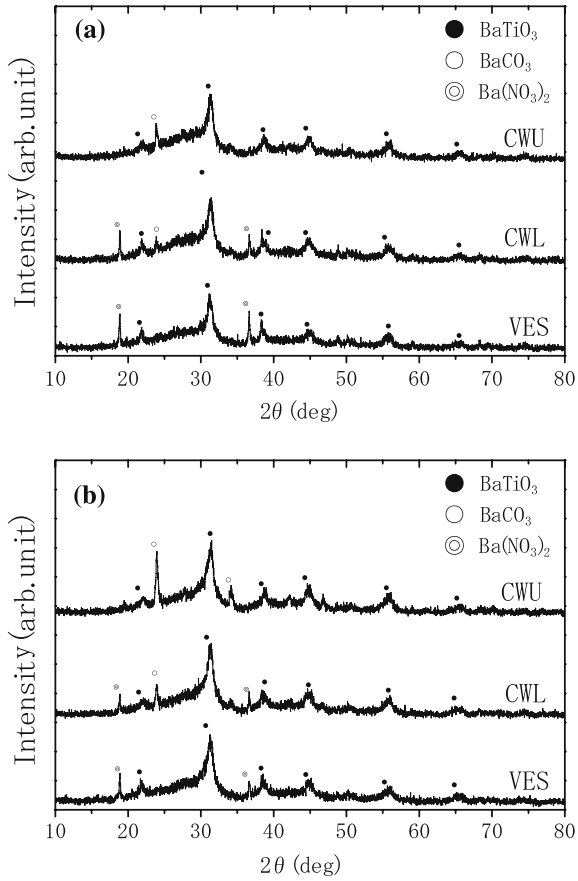

Fig. 4 XRD patterns of the powder products obtained with oxygen injection into the plasma tail flame (CuK_α). In this case, oxygen (1000 SCCM) was introduced into the ICP as a working gas. A water-cooled vessel was used for powder collection. The conditions of oxygen injection are as follows; (a) oxygen-injected position = 340 mm below the ICP and oxygen flow rate = 3500 SCCM (b) oxygen-injected position = 520 mm below the ICP and oxygen flow rate = 3500 SCCM

phase fraction in the VES product and the weight ratio of the VES product, respectively. The average $BaCO_3$ phase and $Ba(NO_3)_2$ phase fractions were similarly calculated.

Figure 5 shows the dependence of the average fraction of the crystalline phases ($BaTiO_3$, $BaCO_3$ and $Ba(NO_3)_2$) on the injected oxygen flow rate. Figure 5 confirms that the average $BaTiO_3$ phase fraction was maximum at an oxygen flow rate of 3500 SCCM at each oxygen-injected position. In this case, the molar concentration of oxygen molecules is approximately 4000 times of the molar concentration of the reactants (=sum of Ba atoms and Ti atoms). An increase of the oxygen flow rate (5000 SCCM) decreased the $BaTiO_3$ fraction, which suggests that a decrease of the temperature of the plasma tail flame due to oxygen injection affects the crystalline phases. These results will be discussed in the section The effect of oxygen injection on the crystalline phase.

An almost single phase of the perovskite $BaTiO_3$ was obtained at the following conditions: O_2 = 3500 SCCM-position = 340 mm ($BaTiO_3$ of 92.5 wt%) and O_2 = 3500 SCCM-position = 520 mm ($BaTiO_3$ of 89.3 wt%). However, the $BaTiO_3$ phase fraction was estimated to be 82.5 wt% at the condition of O_2 = 3500 SCCM-position = 160 mm, and the $BaCO_3$ phase fraction in the products was increased to 17.4 wt%. This indicates that the oxygen-injected position affects the $BaTiO_3$ phase fraction. The relationship between the oxygen-injected position and $BaTiO_3$ fraction in the products will be discussed in the section The most optimized condition of oxygen injection.

In order to obtain perovskite $BaTiO_3$ nanoparticles with a perfect single phase, it is required to accelerate the reaction of the Ba element and increase the crystallization of the amorphous nanoparticles in the plasma tail flame. This will be realized by an increase of the temperature of the plasma tail flame. High temperature of the plasma tail flame can be achieved by means of increasing the output power of the ICP. However, in the present study, the output power of the ICP was fixed at 6.0 kW, which is a relatively low output power. In order to increase the output power of ICP safely, it is necessary to optimize the diameter of quartz reaction tube, because the ICP with high output power has a rather high temperature that often causes the quartz reaction tube to break.

Additionally, the precise control of the Ba/Ti ratio of the reactants is important to prepare perovskite $BaTiO_3$ nanoparticles with a perfect single phase (see section Ba/Ti atomic ratio of the products prepared by oxygen injection).

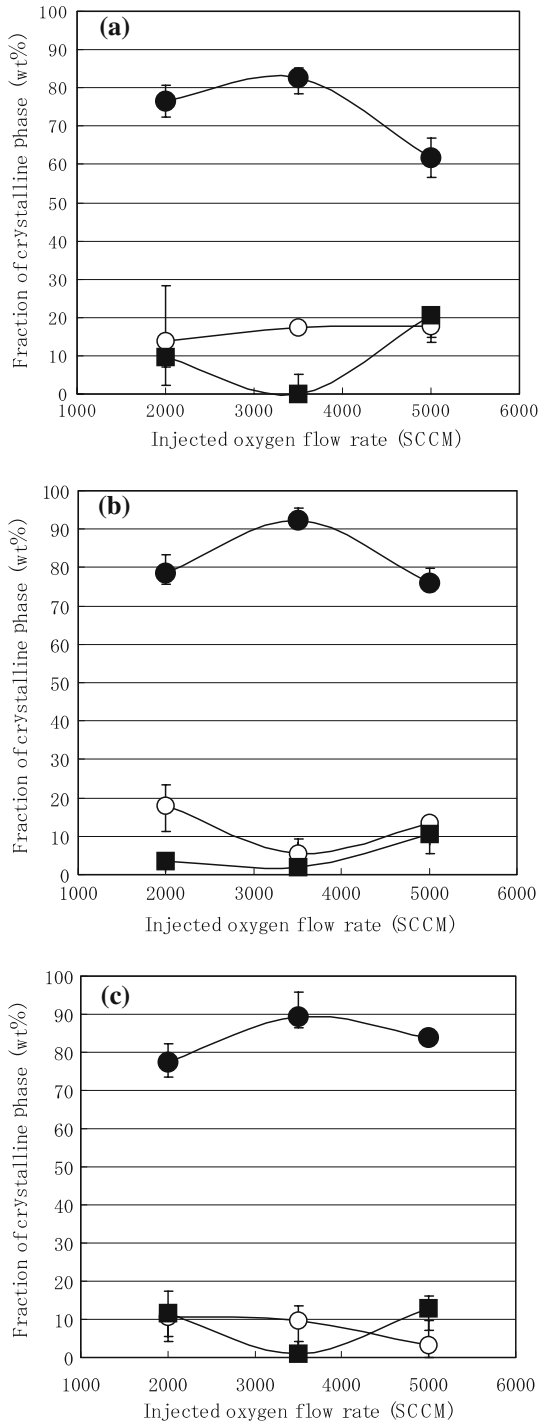

Fig. 5 Dependence of the average fraction of the synthesized phases on the injected oxygen flow rate for each oxygen injection condition. (a) oxygen-injected position = 160 mm (b) oxygen-injected position = 340 mm (c) oxygen-injected position = 520 mm. The symbols of black circles, white circles and black squares represent $BaTiO_3$, $BaCO_3$ and $Ba(NO_3)_2$, respectively

Ba/Ti atomic ratio of the products prepared by oxygen injection

Figure 6 shows the dependence of the Ba/Ti atomic ratio of the products on the oxygen flow rate for each oxygen-injected position (using XRF). In this figure, some of the data have not been presented, because the amounts of the corresponding products were too small to perform the XRF measurement.

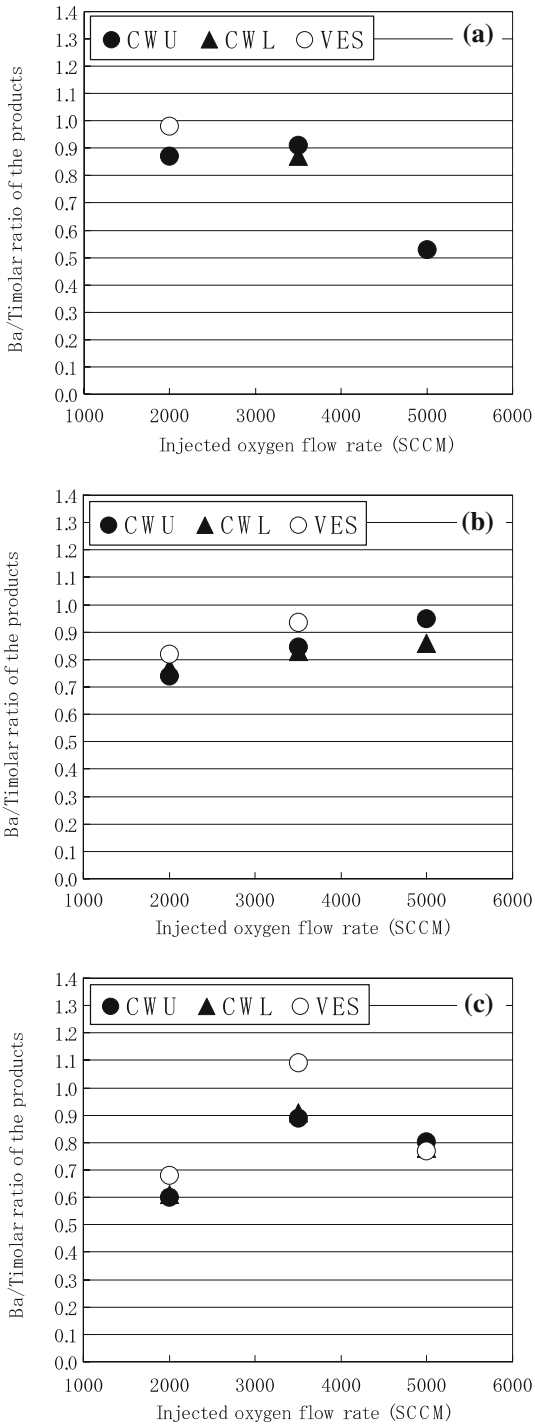

Fig. 6 Dependence of the Ba/Ti atomic ratio of the products on the oxygen flow rate for each oxygen-injected position. The Ba/Ti atomic ratios were investigated by XRF measurements. In this figure, some data are not described, because the amounts of the corresponding products were too small to perform the XRF measurement

The deviations of the Ba/Ti atomic ratios of the products at each collection area were approximately 0.1, therefore the compositions of the products from each area were demonstrated to be equivalent. The Ba/Ti atomic ratios of the products ranged from 0.8 to 1.1 were near stoichiometric composition.

However, the Ba/Ti atomic ratios of the products for the condition: O_2 = 5000 SCCM-position = 160 mm and O_2 = 2000 SCCM-position = 520 mm were approximately 0.6, which is a considerable deviation from the stoichiometric composition. The reason for this phenomenon is supposed as follows. The vapor pressure of $Ba(DPM)_2$ tends to decrease due to repeated heating. Thus, fresh $Ba(DPM)_2$ was periodically added to the source cylinder in order to maintain the vapor pressure of the Ba source. In the present experiments, the powder preparations at the above two conditions were performed just before the addition of fresh $Ba(DPM)_2$. Therefore, the decrease of the Ba/Ti ratio of those products is presumably due to the low vapor pressure of the Ba source materials.

In order to obtain the products with stoichiometric composition, it is necessary to control the Ba/Ti atomic ratio of the source materials that are introduced into the ICP. Monitoring the Ba/Ti atomic ratio of the reactants in the ICP by using optical emission spectroscopy will be an important technique. Furthermore, to substitute raw materials of metalorganics for raw materials of liquid state or solid state will also be effective for controlling the composition of raw materials. The precise control of the Ba/Ti atomic ratio of the products will enable the production of perovskite $BaTiO_3$ nanoparticles with no byproducts and no lattice defects.

According to the XRF measurements, the impurities such as strontium (Sr) of 0.02–0.04 wt%, calcium (Ca) of 0.00–0.04 wt%, iron (Fe) of 0.02–0.08 wt% and nickel (Ni) of 0.03–0.06 wt% were detected from the products. Sr and Ca originate from the barium raw materials. Therefore, using highly pure raw materials will be important to produce highly pure $BaTiO_3$ nanoparticles. It is assumed that Fe and Ni are vaporized from the stainless steel of the reaction chamber due to the high temperature of the plasma tail flame. Coating the stainless steel with heat resisting materials will be effective to prevent the vaporization of Fe and Ni.

TEM observation

The powder products prepared under the condition O_2 = 3500 SCCM-position = 340 mm ($BaTiO_3$ = 92.5 wt%) were observed using a TEM. Figure 7 shows the bright field images and the selected area electron diffractions (SAED) of the products. Figure 7(a), (b) and (c) are photographs of the CWU products, CWL products and VES products, respectively.

The nanoparticles in each image show spherical shapes without crystal habits. The SAED patterns of each product can be indexed to the perovskite single phase of $BaTiO_3$.

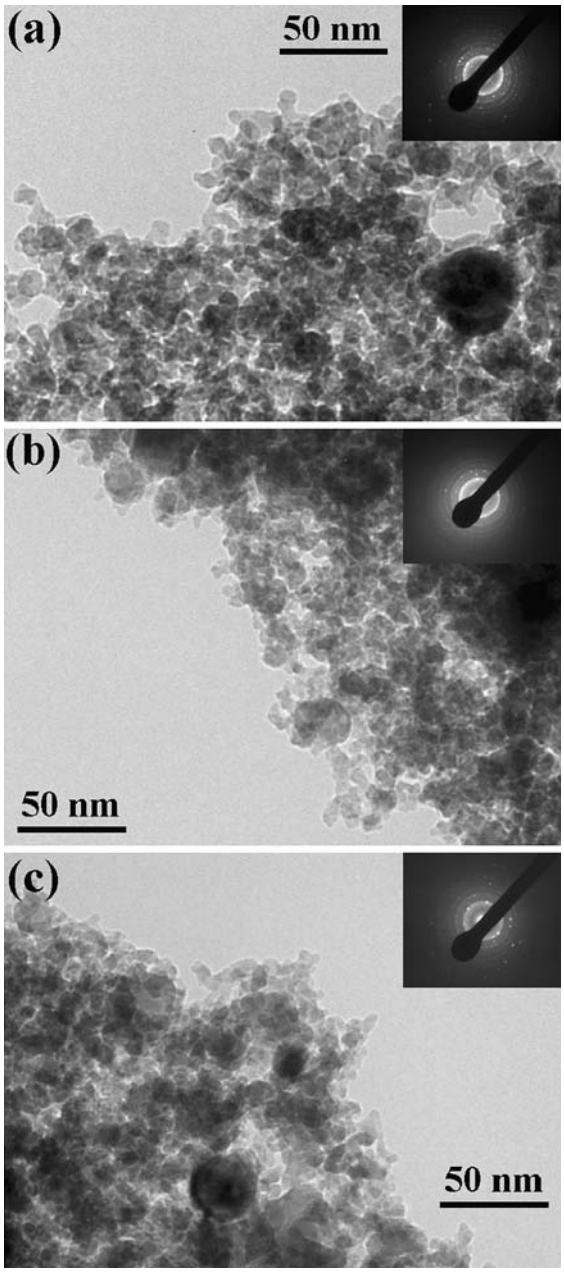

Fig. 7 Bright field TEM images and the corresponding selected area diffractions of the products for each collection area. (a) CWU product (b) CWL product (c) VES product. The powder products prepared at the condition O_2 = 3500 SCCM-position = 340 mm ($BaTiO_3$ = 92.5 wt%) were observed

Therefore, the morphologies and crystal structures of each product were in good agreement.

The shape of multi-component oxide nanoparticles with a complicated crystal structure is reported to be spherical in RF-plasma CVD [23]. In the case of a complicated crystal structure, such as perovskite structure, the crystal growth in the gas stream is supposed to be restrained prior to the generation of crystal habits. The relatively complicated crystal structure of perovskite is assumed to cause the spherical shapes of the $BaTiO_3$ nanoparticles.

Figure 8 shows a high-resolution TEM image of $BaTiO_3$ nanoparticles (the CWL products in Fig. 7). Lattice fringes were clearly observed, suggesting that the $BaTiO_3$ nanoparticles were highly crystallized. Thus, the method of oxygen injection into the plasma tail flame can yield well-crystallized $BaTiO_3$ nanoparticles.

Particle size and size distribution

Particle size distribution of the $BaTiO_3$ nanoparticles was investigated by counting 100 nanoparticles in the bright field TEM images, and the particle sizes were curve-fitted by log-normal function. Figure 9 illustrates the particle size distribution of the VES products shown in Fig. 7(c). As described in this figure, the particle size of the $BaTiO_3$ nanoparticles followed a log-normal distribution. The particle sizes of the $BaTiO_3$ nanoparticles from CWU and CWL were also confirmed to follow a log-normal size distribution.

Ulrich, [24] assuming that the chemical reaction and nucleation times were short compared with the particle growth period by coagulation, showed that the particle size distribution of SiO_2 powders produced by flame oxidation

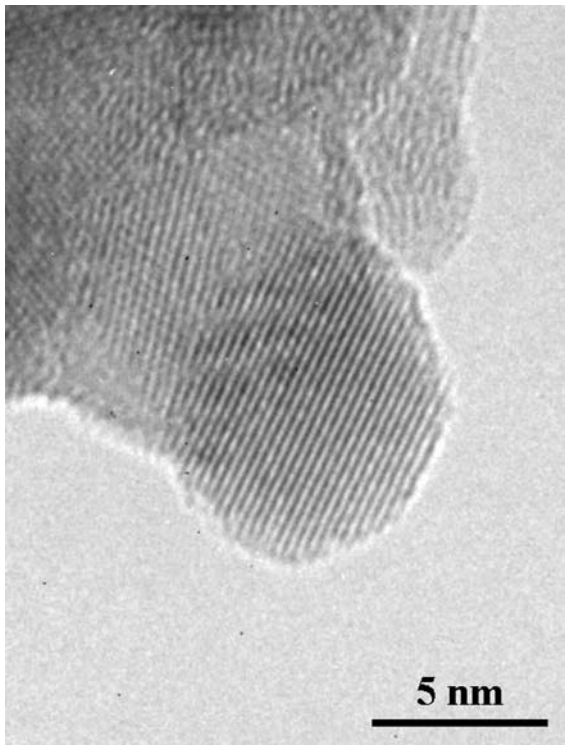

Fig. 8 High-resolution TEM image of the $BaTiO_3$ nanoparticles. The CWL products prepared at the condition O_2 = 3500 SCCM-position = 340 mm ($BaTiO_3$ = 92.5 wt%) were observed

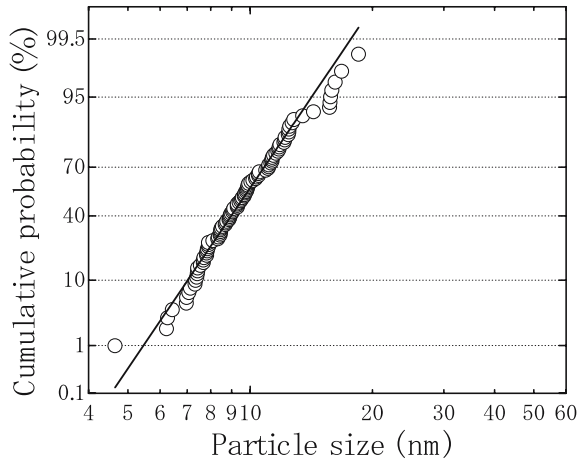

Fig. 9 Particle size distribution of the $BaTiO_3$ nanoparticles (= the VES products in Fig. 7(c)). The particle size distribution was investigated by counting 100 nanoparticles in the bright field TEM images. The particle sizes were curve-fitted using a log-normal function

of $SiCl_4$ was a log-normal distribution. He indicated that the particle growth occurred by the coagulation of liquid droplets, which resulted in the log-normal particle size distribution. This phenomenon was also proved by Cozzi and Cadorin [25]. In RF-plasma CVD, the particle size distributions of Al_2O_3–TiO_2 powder produced by Gani et al. [12] and Y–Fe–O nanoparticles prepared by Sugasawa et al. [20] were observed to be log-normal, which is consistent with Ulrich's model. In the present experiment, the shapes of the nanoparticles were spherical, and the particle size distribution showed log-normal. These results suggest that the $BaTiO_3$ nanoparticles prepared by RF-plasma CVD were formed due to the coagulation of liquid droplets.

On the other hand, Suzuki et al. [7] synthesized a wide variety of single-component oxide nanoparticles by spray-ICP, and indicated that the gas–solid reaction predominantly occurred instead of liquid droplet coagulation, if concentration of reactants was relatively low. However, the feeding rate of Ba and Ti source materials in the present study was calculated to be approximately 5.0×10^{-5} mol/min, which is almost equal to the feeding rate of the spray-ICP (10^{-5}–10^{-4} mol/min) performed by Suzuki et al. Therefore, coagulation processes of liquid droplets can occur in the case of low feeding rates of the raw materials.

Table 3 shows the average particle size D_{50} and geometric standard deviation σ_g of the $BaTiO_3$ nanoparticles from each collection area calculated by log-normal fitting of size distribution. In Table 3, the values without oxygen injection [21] are described for comparison. D_{50} with oxygen injection was estimated to be 8.8 nm (CWU), 8.2 nm (CWL) and 9.5 nm (VES). On the contrary, D_{50} without oxygen injection was estimated to be 15.4 nm. Thus, the downsizing of the $BaTiO_3$ nanoparticles was

Table 3 The average particle sizes D_{50} and geometric standard deviations σ_g of the $BaTiO_3$ nanoparticles prepared under the following condition: O_2 = 3500 SCCM-position = 340 mm ($BaTiO_3$ = 92.5 wt%). For comparison, D_{50} and σ_g without oxygen injection are also described

	D_{50}	σ_g
Oxygen injection		
CWU	8.8 nm	1.27
CWL	8.2 nm	1.25
VES	9.5 nm	1.27
No oxygen injection	15.4 nm	1.32

achieved by oxygen injection into the plasma tail flame. Gani et al. [12] also confirmed that the size of the Al_2O_3–TiO_2 particles decreased by oxygen injection into the plasma tail flame. The downsizing of the nanoparticles can be attributed to the quenching effect caused by oxygen injection.

Discussion

Due to oxygen injection into the plasma tail flame, the same crystalline phases were obtained from all the collection areas. It was also confirmed that the fraction of the crystalline phases ($BaTiO_3$, $BaCO_3$ and $Ba(NO_3)_2$) varied with the conditions of oxygen injection. In the present section, the effects of oxygen injection on the crystalline phases and the most optimized condition of oxygen injection are discussed.

Prior to the discussion, a measurement of the temperature of the plasma tail flame at the oxygen-injected position is necessary. The temperature measurement was performed by inserting a thermocouple into the plasma tail flame. A Pt–PtRh (Rh13 wt%) thermocouple and an alumel–chromel thermocouple were used for the measurement. Because of the heat transfer from the plasma tail flame to the thermocouple, the temperature measured by the thermocouple should be lower than the actual temperature of the plasma tail flame. However, it is difficult to estimate the actual temperature of the plasma tail flame, therefore the temperature measured by the thermocouple was defined as the temperature of the plasma tail flame. Table 4 shows the temperatures of the plasma tail flame at the oxygen-injected positions. Using these temperatures, the relationship between the oxygen injection condition and crystalline phases is discussed.

The effect of oxygen injection on the crystalline phase

As mentioned above, $BaTiO_3$ was deposited on the sidewalls of the reaction chamber, whereas $Ba(NO_3)_2$ was obtained from a water-cooled vessel without oxygen

Table 4 Temperatures of the plasma tail flame at the oxygen-injected position. The temperature measurement was performed by inserting a thermocouple into the plasma tail flame. A Pt - PtRh (Rh13wt%) thermocouple and an alumel–chromel thermocouple were used. Because of the heat transfer from the plasma tail flame to the thermocouple, the temperature measured by the thermocouple should be lower than the real temperature of the plasma tail flame. However, it is difficult to estimate the real temperature of the plasma tail flame, therefore the temperature measured by the thermocouple was defined as the temperature of the plasma tail flame in the present study

	2000 SCCM	3500 SCCM	5000 SCCM
160 mm	1585 K	1445 K	1345 K
340 mm	1135 K	995 K	895 K
520 mm	990 K	850 K	750 K

injection (see Fig. 3). However, the $Ba(NO_3)_2$ phase vanished and $BaTiO_3$ phase appeared in the water-cooled vessel by oxygen injection into the plasma tail flame.

In order to discuss the present results quantitatively, equilibrium phases for various oxygen injection conditions were thermodynamically investigated. The software CEA600 provided by NASA Glenn Research Center [26] was employed for thermodynamical calculation. The minimization of free energy formulation is used in the CEA600 program. This method has an advantage that each species can be treated independently without specifying a set of reactions. The thermodynamic data used in this program were selected from several sources such as ''JANAF Thermochemical Tables'' [27], ''CODATA Key Values for Thermodynamics'' [28] and ''TRC Thermodynamic Tables'' [29].

The calculations were performed on the basis of the experimental conditions shown in Table 1. The temperature was varied from 300 K (room temperature) to 1900 K (the temperature at which the nucleation of $BaTiO_3$ occurs), and the pressure was kept constant at 4.0 kPa. An introduction rate of the reactants was calculated by measuring the weight loss of each source bubbler after synthesis. Nitrogen was estimated by a leak test of the reaction chamber ($=1.8 \times 10^{-3}$ mol/h). The atomic ratio of the reactants, nitrogen and argon is as follows: Ba:Ti:C:H:N:Ar = 1:1:34:66:3:9469. The oxygen of 1000 SCCM introduced as a working gas was also considered in the calculation under each condition.

Figure 10 shows thermodynamically predicted equilibrium composition without oxygen injection into the plasma tail flame. The chemical species in the thermodynamically predicted equilibrium state were as follows: Ar, O_2, CO_2, H_2O, N_2, OH, NO, NO_2, $BaCO_3$, TiO_2 and $BaTiO_3$. For simplicity, the relevant phases of $BaTiO_3$, $BaCO_3$, TiO_2, N_2, NO and NO_2 have been attached in Fig. 10. At 1900 K, the solid phase of $BaTiO_3$ precipitated and the gas phases of N_2, NO_2 and NO with almost the same amounts of the

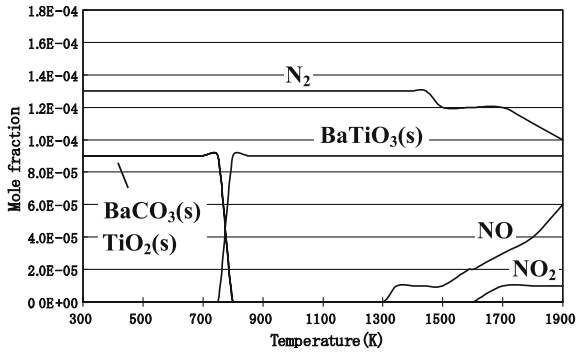

Fig. 10 Thermodynamically predicted equilibrium compositions of the chemical species without oxygen injection into the plasma tail flame. Software CEA600 provided by NASA Glenn Research Center [26] was employed for calculation. The calculations were performed on the basis of the experimental conditions shown in Table 1. The temperature ranged from 300 K to 1900 K, and the pressure was kept constant at 4.0 kPa. Nitrogen leakage rate was estimated from a leak test of the reaction chamber ($=1.8 \times 10^{-3}$ mol/h), and the contribution of nitrogen to the reaction was taken into account. An introduction rate of the reactants was calculated by measuring the weight loss of each source bubbler after synthesis. The atomic ratio of the reactants, nitrogen and argon is as follows: Ba:Ti:C:H:N:Ar = 1:1:34:66:3:9469. The oxygen of 1000 SCCM introduced as a working gas was also considered. For simplicity, the main phases such as $BaTiO_3$, $BaCO_3$, TiO_2, N_2, NO and NO_2 were inserted in the figure

$BaTiO_3$ phase existed. NO_2 and NO decomposed into N_2 and O_2 at 1600 K and 1300 K, respectively. The gas phase of Ba did not exist, which indicates that the gas phase of Ba is not an equilibrium phase. The solid phase of $BaTiO_3$ decomposed into $BaCO_3$ and TiO_2 at 800 K. Consequently, the $BaCO_3$ phase and the TiO_2 phase were identified with equilibrium phases at room temperature, and the $Ba(NO_3)_2$ phase was not confirmed as an equilibrium phase. Accordingly, $Ba(NO_3)_2$ deposited on the water-cooled vessel, as shown in Fig. 3, is considered to be a non-equilibrium phase produced by the plasma process. As mentioned in the section Crystalline phases without oxygen injection into the plasma tail flame, the active Ba atoms deposited on the water-cooled vessel are supposed to react with nitrogen and oxygen, and then transform to the $Ba(NO_3)_2$ phase, when the reaction chamber is exposed to air for powder collection.

Figure 11 shows the thermodynamically predicted equilibrium compositions of the chemical species for various oxygen injecting conditions shown in Table 2. In the figure, the dotted line represents the temperature of the plasma tail flame at the oxygen-injected position. The oxygen injection increased the oxygen concentration in the reaction system, and caused a decrease in the relative concentration of N_2 and $BaTiO_3$. In the case of oxygen injection at the position = 160 mm, the decomposition temperature of NO and NO_2 became lower than that in the case of no-oxygen injection (Fig. 10). Except for lowering

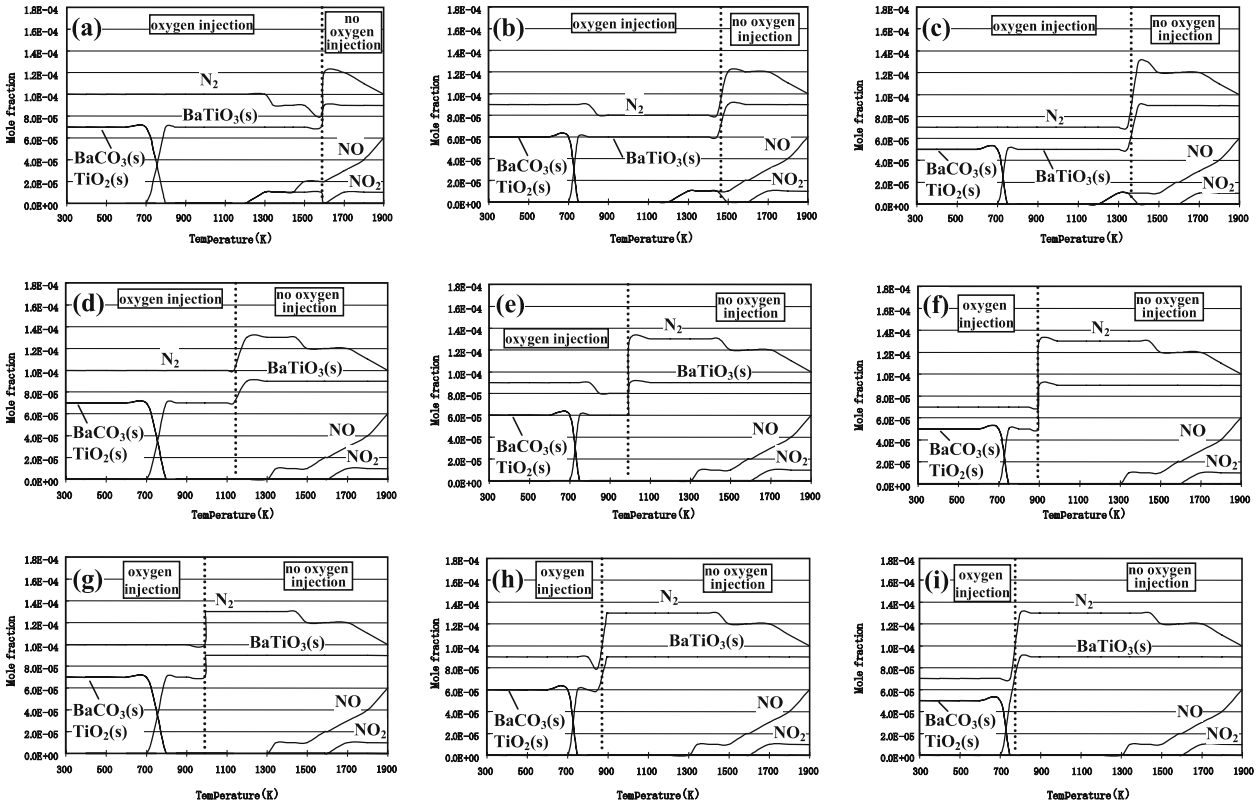

Fig. 11 Thermodynamically predicted equilibrium compositions of chemical species for various oxygen injection conditions shown in Table 2. (a) O_2 = 2000 SCCM-position = 160 mm (b) O_2 = 3500 SCCM-position = 160 mm (c) O_2 = 5000 SCCM-position = 160 mm (d) O_2 = 2000 SCCM-position = 340 mm (e) O_2 = 3500 SCCM-position = 340 mm (f) O_2 = 5000 SCCM-position = 340 mm (g) O_2 = 2000 SCCM-position = 520 mm (h) O_2 = 3500 SCCM-position = 520 mm (i) O_2 = 5000 SCCM-position = 520 mm. In the figure, the dotted line means the temperature of the plasma tail flame at oxygen injection position. For simplicity, the relevant phases such as $BaTiO_3$, $BaCO_3$, TiO_2, N_2, NO and NO_2 were inserted. The oxygen of 1000 SCCM introduced through a working gas line was also considered in the calculation under all conditions

of the decomposition temperature of NO and NO_2, the result of the thermodynamic calculation in the case of oxygen injection did not exhibit remarkable changes compared with that in the case of no-oxygen injection. $BaCO_3$ and TiO_2 were identified with thermodynamical equilibrium phases at room temperature under all conditions. Although the experimentally produced phase with oxygen injection was $BaTiO_3$, the thermodynamically calculated phase was not $BaTiO_3$. These results reveal that the effect of oxygen injection cannot be explained by thermodynamical calculations. Since the chemical reaction time in the present synthesis is about 50 ms, a quasi-static process in thermodynamics is not applicable to the plasma process.

Therefore, chemical kinetics was used to explain the effects of oxygen injection. Essentially, a wide variety of chemical reactions such as

$$\mathrm{Ba} + \mathrm{TiO_2} + 1/2\mathrm{O_2} \rightarrow \mathrm{BaTiO_3} \tag{2}$$

$$\mathrm{Ba} + \mathrm{CO_2} + 1/2\mathrm{O_2} \rightarrow \mathrm{BaCO_3} \tag{3}$$

$$\mathrm{Ba} + \mathrm{N_2} + 3\mathrm{O_2} \rightarrow \mathrm{Ba(NO_3)_2} \tag{4}$$

should be taken into account for the calculations. However, no experimental data exist for velocity constants concerned with above reactions. Thus, only the following reaction was considered in the present discussion.

$$\mathrm{Ba} + \mathrm{O_2} \rightarrow \mathrm{BaO} + \mathrm{O} \tag{5}$$

The velocity constant associated with reaction (5) has been measured by Kashireninov et al. [30].

The $Ba(NO_3)_2$ phase fraction is supposed to decrease with an increase in the reaction velocity of Eq. (5) by oxygen injection into the plasma tail flame. The reaction velocity of Eq. (5) is described as follows.

$$\frac{\mathrm{d[BaO]}}{\mathrm{d}t} = k_{\mathrm{BaO}} \cdot [\mathrm{Ba}] \cdot [\mathrm{O_2}] \tag{6}$$

Here, d[BaO]/dt, k_{BaO}, [Ba] and [O] show the reaction velocity, the velocity constant, the concentration of barium

atoms and the concentration of oxygen molecules, respectively. Furthermore, k_{BaO} is described as follows [30],

$$k_{BaO} = A \cdot \exp\left(\frac{-E_a}{RT}\right) = 2.0 \times 10^8 \cdot \exp\left(\frac{-50635}{RT}\right) \quad (7)$$

where, A represents a frequency factor (unit: m^3/mol/s), and E_a represents an activation energy (unit: J/mol). By substituting Eq. (7) into Eq. (6), the reaction velocity d[BaO]/dt was obtained.However, the estimation of [Ba] is actually difficult. Therefore, in the present calculation, it was assumed that [Ba] is constant. Moreover, oxygen flow rate (Q_{O_2}) was substituted for [O_2], because the calculated reaction velocities can be relatively compared. Thus, d[BaO]/dt is proportional to the product of k_{BaO} (function of temperature) and Q_{O_2} (function of oxygen concentration). Here, the product of k_{BaO} and Q_{O_2} is defined as d[BaO]′/dt.

$$\frac{d[BaO]'}{dt} \equiv k_{BaO}\, Q_{O_2} \quad (8)$$

Namely, increases of the temperature of the plasma tail flame and of the oxygen concentration lead to an increase in the reaction velocity of Eq. (5).Figure 12 shows the dependence of the fraction of $Ba(NO_3)_2$ in the water-cooled vessel on d[BaO]′/dt. Since the velocity constant of Eq. (5) is available in the range from 970 K to 1180 K [27], the corresponding temperatures in Table 4 (the following conditions; O_2 = 2000 SCCM-position = 340 mm (1135 K), O_2 = 3500 SCCM-position = 340 mm (995 K) and O_2 = 2000 SCCM-position = 520 mm (990 K)) were used in the calculations.As shown in Fig. 12, the fraction of $Ba(NO_3)_2$ decreased as d[BaO]′/dt increased. The d[BaO]′/dt of 8.5×10^8, 14.4×10^8 and 18.6×10^8 corresponds to the condition O_2 = 2000 SCCM-position = 520 mm (990 K), O_2 = 3500 SCCM-position = 340 mm (995 K) and O_2 = 2000 SCCM-position = 340 mm (1135 K), respectively. This result demonstrates that the increases of temperature and oxygen concentration, namely, the increase of the reaction velocity of Eq. (5), resulted in a decrease of the $Ba(NO_3)_2$ phase. Hence, the effect of oxygen injection into the plasma tail flame can be ascribed to the increase of the reaction velocity of Ba oxidation.However, the above calculation was carried out using a rather simplified model. The consideration of parameters such as the velocity constants of Eqs. (2)–(4), the reaction time and the concentration of Ba atoms is necessary for precise evaluation of the chemical reactions in the plasma tail flame.

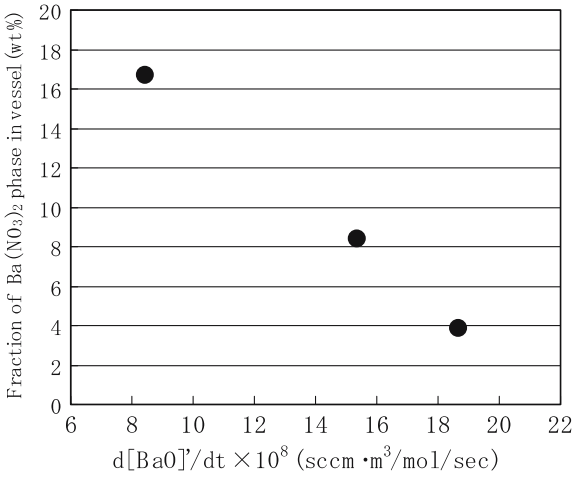

Fig. 12 Dependence of the fraction of $Ba(NO_3)_2$ in a water-cooled vessel on d[BaO]′/dt (here, d[BaO]$\prime$/d$t \equiv k$ BaO $\times$ Q_{O_2}). Since the velocity constant of Eq. (4) is available in the range from 970 K to 1180 K [27], the corresponding temperatures in Table 4 were used for the calculations. The d[BaO]′/dt of 8.5×10^8, 14.4×10^8 and 18.6×10^8 corresponds to the condition O_2 = 2000 SCCM-position = 520 mm (990 K), O_2 = 3500 SCCM-position = 340 mm (995 K) and O_2 = 2000 SCCM-position = 340 mm (1135 K), respectively

The most optimized condition of oxygen injection

As shown in Fig. 5, the $BaTiO_3$ fractions for oxygen-injected positions of 340 mm and 520 mm were confirmed to be higher than those for the position of 160 mm. This relationship suggests that the $BaTiO_3$ fraction is associated with the temperatures of the plasma tail flame at the oxygen-injected positions.

Figure 13 shows the relationship between the average $BaTiO_3$ fractions and the temperatures of the plasma tail flame at the oxygen-injected positions. The $BaTiO_3$

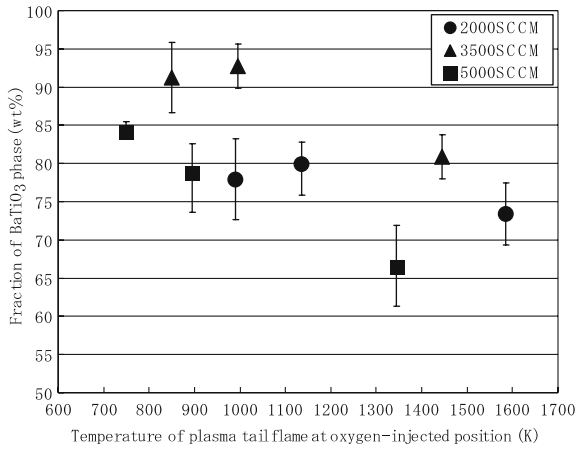

Fig. 13 Relationship between the average $BaTiO_3$ fractions and the temperatures of the plasma tail flame at oxygen-injected positions. The fraction of the $BaTiO_3$ phases was calculated by XRD peak intensities using the internal standard method

fractions gradually decreased with the increase of the temperature of the plasma tail flame at each oxygen flow rate.

Thermodynamical calculation by CEA600 [26] reveals that the solidification temperature of $BaTiO_3$ is approximately 1900 K, which implies that $BaTiO_3$ begins to nucleate above the oxygen-injected position. If the oxygen is injected at a position of high temperature region (i.e. close to the plasma), the crystal growth of $BaTiO_3$ will be restrained because of the cooling of the plasma tail flame. On the contrary, the nucleation and the growth of $BaTiO_3$ will proceed without interference, if the oxygen is injected at a position in a region of relatively low temperature (i.e. far from the plasma). Figure 14 shows a schematic drawing of this phenomenon. Oxygen injection into a relatively low temperature region (=approximately 1000 K) leads to an increase of the $BaTiO_3$ fraction of the products deposited on the water-cooled vessel.

The optimization of oxygen concentration is discussed as follows. The $BaTiO_3$ fraction was confirmed to be maximum at an oxygen flow rate of 3500 SCCM, whereas the $BaTiO_3$ fraction decreased at oxygen flow rates of 2000 SCCM and 5000 SCCM (Fig. 5). The ratio of the oxygen concentration to the concentration of the reactants (=O_2/(Ba+Ti)) was estimated to be 900, 2680, 4000 and 5350 at injected oxygen flow rates of 0 SCCM, 2000 SCCM, 3500 SCCM and 5000 SCCM, respectively. Accordingly, the most efficient fabrication of $BaTiO_3$ will be achieved when O_2/(Ba+Ti) = 4000. When O_2/(Ba+Ti) < 4000, Ba atoms in the plasma tail flame will not react sufficiently with oxygen, because of the low concentration of oxygen. On the other hand, when O_2/(Ba+Ti) > 4000, the production efficiency of $BaTiO_3$ will decrease in spite of the sufficient concentration of oxygen, because the temperature of the plasma tail flame significantly decreases due to the cooling effect. If O_2/(Ba+Ti) > 4000 is achieved by introducing oxygen as the working gas without oxygen injection, the efficiency of $BaTiO_3$ formation should increase.

For stable preparation of $BaTiO_3$ nanoparticles by oxygen injection into the plasma tail flame, oxygen injection with O_2/(Ba+Ti) of approximately 4000 to the low temperature region of the plasma tail flame (approximately 1000 K) is necessary.

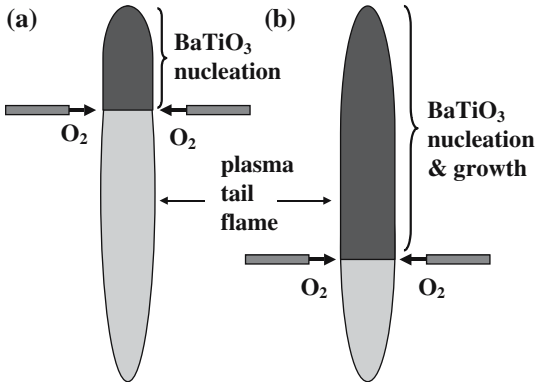

Fig. 14 Schematic drawing of the nucleation and growth of $BaTiO_3$ in the plasma tail flame

Conclusion

In the present study, $BaTiO_3$ nanoparticles with a perovskite phase were synthesized in all collection areas by RF-plasma CVD using oxygen injection into the plasma tail flame. For an efficient fabrication of the $BaTiO_3$ phase, the following conditions are necessary: O_2/(Ba+Ti) = 4000 and the temperature of the plasma tail flame at the oxygen-injected position = approximately 1000 K. The establishment of the synthesis technique of $BaTiO_3$ nanoparticles by RF-plasma CVD will benefit the industry as well as science.

Moreover, an oxygen injection method resulted in the fabrication of $BaTiO_3$ nanoparticles less than 10 nm. The average sizes of the $BaTiO_3$ nanoparticles prepared by oxygen injection were confirmed to be approximately 8 nm, whereas the particle size of the $BaTiO_3$ nanoparticles without oxygen injection was approximately 15 nm. The $BaTiO_3$ nanoparticles were identified to be well-crystallized particles by TEM observation. The spherical shape and the log-normal size distribution of the $BaTiO_3$ nanoparticles suggest that the particles were formed by coalescence of liquid droplets in the gas stream.

References

1. Reed TB (1961) J Appl Phys 32:821
2. Kijima K, Konishi M (1985) J Ceram Soc Japan(Yogyo-Kyokai-Shi) 93:511
3. Hollabough CH, Hull DE, Newkirk LR, Petrovic JJ (1983) J Mater Sci 18:3190
4. Yoshida T, Tani T, Nishimura H, Akashi K (1983) J Appl Phys 54:640
5. Canteloup J, Mocellin A (1976) J Mater Sci 11:2352
6. Tani T, Yoshida T, Akashi K (1986) J Ceram Soc Japan(Yogyo-Kyokai-Shi) 94:11
7. Suzuki M, Kagawa M, Syono Y, Hirai T (1992) J Mater Sci 27:679
8. Kagawa M, Kikuchi M, Ohno R, Nagae T (1981) J Am Ceram Soc 64:C7
9. Hasegawa M, Kato Y, Kagawa M, Syono Y (1996) J Mater Sci 15:1608
10. Kagawa M, Ohta H, Komatsu H, Syono Y (1985) Jpn J Appl Phys 24:477
11. Gani MSJ, McPherson R (1977) J Mater Sci 12:999
12. Gani MSJ, McPherson R (1980) J Mater Sci 15:1915
13. Barry TI, Bayliss RK, Lay LA (1968) J Mater Sci 3:229

14. McPherson R (1973) J Mater Sci 8:859
15. Kagawa M, Kikuchi M, Syono Y, Nagae T (1983) J Am Ceram Soc 66:751
16. Kagawa M, Imamura Y, Usui S, Syono Y (1984) J Mater Sci Lett 3:699
17. Barry TI, Bayliss RK, Lay LA (1968) J Mater Sci 3:239
18. Ono T, Kagawa M, Syono Y (1985) J Mater Sci 20:2483
19. Kagawa M, Suzuki M, Mizoguchi Y, Hirai T, Syono Y (1993) J Aerosol Sci 24:349
20. Sugasawa M, Kikukawa N, Ishikawa N, Kayano N, Kimura T (1998) J Aerosol Sci 29:675
21. Suzuki K, Kijima K (2004) Mater Lett 58:1650
22. Suzuki K, Kijima K (2004) J Ceram Soc Japan Suppl 112:S916
23. Kagawa M (1995) Aerosol Res 10:20
24. Ulrich G (1971) Comb Sci Tech 4:47
25. Cozzi C, Cadorin C (1972) Comb Sci Tech 5:213
26. Gordon S, McBride BJ (1994) In: NASA Reference Publication. NASA Lewes Research Center. p 1311
27. Chase MW, Davies CA, Downey JR, Frurip DJ, McDonald RA, Syverud AN (1985) In: JANAF Thermochemical Tables, American Chemical Society
28. Cox JD, Wagman DD, Medvedev VA (1989) In: CODATA Key Values for Thermodynamics, Hemisphere Publishing Corp
29. Marsh KN, Das A, Frenkel M, Gadalla NM, Wilhoit RC (1988) In: TRC Thermodynamic Tables, Non-Hydrocarbons, vols. I–III, Thermodynamics Research Center, Texas A&M University
30. Kashireninov OE, Kuznetsov VA, Manelis GB (1977) AAIA J 15:1035